

SEAL-pose: Enhancing 3D Human Pose Estimation via a Learned Loss for Structural Consistency

Yeonsung Kim^{1*} Junggeun Do^{2*} Seunguk Do¹ Sangmin Kim¹ Jaesik Park¹ Jay-Yoon Lee¹

Abstract

3D human pose estimation (HPE) is characterized by intricate local and global dependencies among joints. Conventional supervised losses are limited in capturing these correlations because they treat each joint independently. Previous studies have attempted to promote structural consistency through manually designed priors or rule-based constraints; however, these approaches typically require manual specification and are often non-differentiable, limiting their use as end-to-end training objectives. We propose SEAL-pose, a data-driven framework in which a learnable loss-net trains a pose-net by evaluating structural plausibility. Rather than relying on hand-crafted priors, our joint-graph-based design enables the loss-net to learn complex structural dependencies directly from data. Extensive experiments on three 3D HPE benchmarks with eight backbones show that SEAL-pose reduces per-joint errors and improves pose plausibility compared with the corresponding backbones across all settings. Beyond improving each backbone, SEAL-pose also outperforms models with explicit structural constraints, despite not enforcing any such constraints. Finally, we analyze the relationship between the loss-net and structural consistency, and evaluate SEAL-pose in cross-dataset and in-the-wild settings.

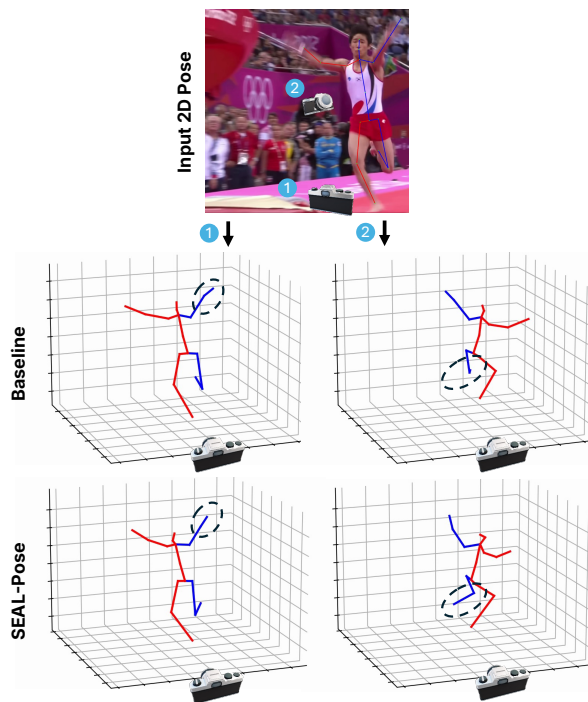


Figure 1. SEAL-pose improves structural consistency by preserving skeletal symmetry and kinematic connectivity; under the same 2D input, KTPFormer (baseline) can exhibit local joint inconsistencies (e.g., ankle/wrist) that propagate to the overall limb configuration.

1. Introduction

3D human pose estimation (3D HPE) requires predicting accurate joint positions while preserving the underlying anatomical structure (Liu et al., 2024). This task is particularly difficult because the output space is governed by com-

plex local and global dependencies between joints. However, common training objectives such as mean squared error (MSE) and mean per-joint position error (MPJPE) penalize individual joint errors without accounting for structural consistency, which often results in implausible or anatomically inconsistent poses. Therefore, it is critical to effectively model the structures in the output space to predict accurate and plausible 3D poses. Previous studies (Zheng et al., 2020; Wu et al., 2022; Fang et al., 2018; Xu et al., 2022; Kim & Lee, 2024) have attempted to capture such structural dependencies using hand-crafted constraints, which can fail to reflect the natural structural consistency of human poses.

To overcome these limitations, we propose SEAL-pose, a framework that provides structural guidance for 3D pose estimation via a trainable loss. Building on Structured En-

*Equal contribution ¹Seoul National University, South Korea ²Texas A&M University, College Station, Texas, USA. Correspondence to: Jaesik Park <jaesik.park@snu.ac.kr>, Jay-Yoon Lee <lee.jayyoon@snu.ac.kr>.

ergy As Loss (SEAL) (Lee et al., 2022), we adapt learnable energy-based loss to 3D human pose estimation, where the output is a high-dimensional 3D geometry constrained by skeletal topology. At the core of SEAL-pose is a skeleton-aware loss-net jointly optimized with a pose estimation model (pose-net). Leveraging skeletal topology as an inductive bias, the loss network learns local and global structural relations—from adjacent joints to long-range dependencies—directly from data. We construct joint-wise coupled 2D–3D inputs for the loss-net, providing observation-conditioned signals that it can aggregate across joints to capture structural plausibility beyond per-joint regression. Although alternating optimization between the pose-net and loss-net can seem to be brittle, a simple greedy hyperparameter tuning shows a reliable convergence of SEAL-pose in practice.

Finally, to evaluate structural quality beyond standard errors such as MPJPE, we introduce two complementary metrics—Limb Symmetry Error (LSE) and Body Segment Length Error (BSLE)—that quantify symmetry and segment-length consistency of predicted poses. Our framework is model-agnostic and easily extends to single-frame, multi-frame, and diffusion-based pose estimation models by simply incorporating the loss network during training. Extensive experiments on Human3.6M (Ionescu et al., 2014), MPI-INF-3DHP (Mehta et al., 2017), and Human3.6M 3D WholeBody (Zhu et al., 2023) demonstrate that SEAL-pose not only reduces per-joint errors (Table 1, 2, 3) but also produces more plausible poses, evaluated by the newly proposed LSE and BSLE (Table 4 and Figure 4, 5). In summary, the contributions of this paper are as follows:

- (i) We redesign SEAL for 3D pose estimation and propose SEAL-pose to bridge the gap between previous discrete label–space dependency modeling and continuous 3D geometric outputs governed by skeletal constraints.
- (ii) We introduce a skeleton-aware graph loss-net with joint-wise 2D–3D coupled representations, and demonstrate consistent improvements across datasets and backbones with no test-time overhead.
- (iii) We propose structure-aware evaluation metrics (LSE/BSLE) and further explore leveraging diverse hypotheses as negative samples, which provides additional gains in both single-frame and multi-frame settings.

2. Related Work

2.1. 3D Human Pose Estimation

3D human pose estimation is a well-established computer vision task involving the prediction of 3D joint positions from 2D images or videos. This task is inherently challenging

because it requires inferring spatial relationships while ensuring anatomical plausibility from incomplete visual information. Current approaches generally follow two paradigms: (1) directly predicting 3D poses from images (Pavlakos et al., 2017; 2018) or (2) estimating 2D poses first and then lifting them to 3D space (Zheng et al., 2023; Liu et al., 2024). The 2D-to-3D lifting has been widely adopted due to progress in 2D human pose estimation (Zheng et al., 2023).

While single frame models such as SimpleBaseline (Martinez et al., 2017) and SemGCN (Zhao et al., 2019) perform well, they process frames independently and thus cannot enforce temporal consistency, often resulting in jitter. This limitation has motivated multi-frame models that leverage temporal dynamics for more stable and robust 3D pose estimation.

Transformer-based models. Transformers (Vaswani et al., 2023) have become a major backbone for 3D human pose estimation. PoseFormer (Zheng et al., 2021) was the first transformer-based architecture for this task, and PoseFormerV2 (Zhao et al., 2023) improved efficiency via frequency-domain representations. While PoseFormer-style models typically handle spatial relations before temporal modeling, MixSTE (Zhang et al., 2022) interleaves the two through a mixed spatio-temporal encoder. P-STMO (Shan et al., 2022) further introduces a pre-trained spatio-temporal masked autoencoder to capture motion dynamics efficiently. To incorporate skeletal priors into self-attention, MotionAGFormer (Mehraban et al., 2024) combines GCNs with Transformers, whereas KTPFormer (Peng et al., 2024) injects kinematic and trajectory priors to stabilize attention.

Graph-based models. Graph-based models, such as Graph Convolutional Networks (Kipf & Welling, 2017) and Graph Attention Networks (Veličković et al., 2018), are widely used in human pose estimation because they naturally encode skeletal structure (Zhao et al., 2019), but their local receptive fields limit long-range reasoning. Graformer addresses this by injecting joint and edge-aware priors into the attention mechanism, enabling global, structure-aware interactions (Zhao et al., 2022). Building on this idea, we design a structure-aware loss-net that guides the pose-net to learn the human kinematic structure consistently.

2.2. Output Structure of 3D HPE

3D HPE has inherent challenges such as ambiguity due to incomplete information, which is further compounded in single-frame scenarios. To address this issue, previous works have designed methods that consider prior knowledge of human body structure and joint relationships (Fang et al., 2018; Xu et al., 2022; Zheng et al., 2020; Chen et al., 2022), and enforced structural plausibility by explicitly constraining bone length, angles, and symmetry (Cao & Zhao, 2021; Wu et al., 2022; Bigalke et al., 2022; Chen et al., 2022).

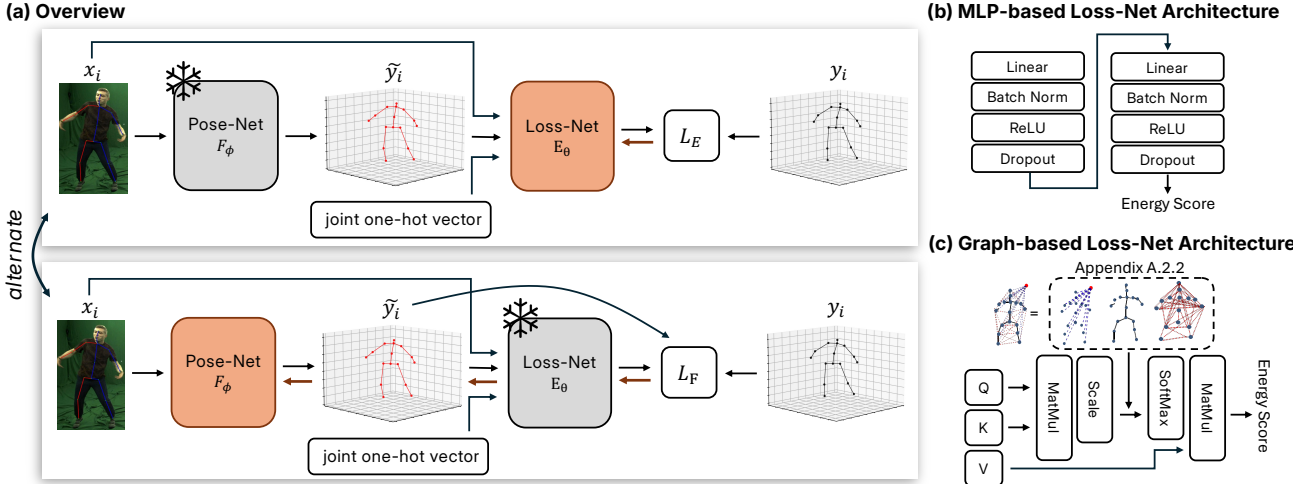


Figure 2. (a) **Overview of SEAL-pose.** SEAL-pose combines a pose-net F_ϕ that lifts 2D keypoints x_i to a predicted 3D keypoints \tilde{y}_i with a loss-net E_θ (graph-based or MLP) that predicts an energy score, where y_i denotes the ground-truth 3D pose. It adopts **alternating optimization**: it first freezes E_θ and optimizes F_ϕ to minimize the energy of predicted poses. Then, it freezes F_ϕ and trains E_θ so that its energy better reflects pose quality. (b-c) **Loss-net Architecture Variants.**

Beyond these approaches, recent studies have explored generating multiple hypotheses or plausible 3D poses to alleviate depth ambiguity and structural uncertainty. For instance, (Kim & Lee, 2024) proposed a Biomechanical Pose Generator to augment training data with biomechanically valid poses, along with Binary Depth Coordinates to resolve the depth ambiguity by classifying the joint depths as front or back. Similarly, (Rommel et al., 2024) introduced ManiPose, a manifold-constrained multi-hypothesis approach that estimates the plausibility of each candidate and restricts them to the human pose manifold.

Despite their contributions, most existing methods rely on prior knowledge or predefined rules, which may limit scalability and adaptability. In contrast, we aim to address these limitations by providing a more flexible and general approach for 3D HPE that captures joint dependencies without explicit prior knowledge. In addition, our method, SEAL-pose, is agnostic to model architecture and can potentially be extended to various tasks with complex output structures.

3. Methodology

3.1. Preliminaries: Structured Energy as Loss (SEAL)

The Structured Energy As Loss (SEAL) framework improves structured prediction by using a structured energy network as a trainable loss. Concretely, SEAL introduces a secondary network (loss-net) that scores the plausibility of a model’s outputs, and uses this score to provide learning signals for the primary predictor (task-net). This formulation encourages the task-net to account for dependencies among output variables without relying on handcrafted constraints.

SEAL is commonly instantiated in two variants: SEAL-static and SEAL-dynamic. SEAL-static uses a fixed, pre-trained loss-net during training, while SEAL-dynamic updates the loss-net jointly as the pose-net evolves. Prior work reports that SEAL-dynamic often yields stronger supervision than SEAL-static. Accordingly, we adopt the SEAL-dynamic formulation in our framework.

3.2. Designing SEAL for 3D HPE.

Unlike the discrete structured output spaces typically considered in SEAL, 3D human pose estimation operates in a continuous, high-dimensional coordinate space. In this setting, structure is expressed as geometric relationships on the human skeleton. To make a trainable loss effective in this setting, we design SEAL-pose around three choices. First, we implement the loss-net as a skeleton-aware, graph-based model to capture both local and global joint relationships. Second, we design and evaluate loss-net input representations to tackle the non-trivial challenge of learning compatibility between 2D and 3D skeletal points in a continuous geometric space. Third, we introduce synthetic negatives to strengthen the loss net’s training signal in deterministic 3D HPE models, which lack the natural diversity of negatives available in probabilistic formulations considered in Lee et al. (2022).

3.3. Training Procedure.

Our framework consists of two components: (i) pose-net, which can be any 3D HPE model that predicts 3D joint positions from 2D inputs, and (ii) loss-net, a trainable loss function that dynamically learns to evaluate the structural

Algorithm 1 SEAL-pose Algorithm

Require: (\mathbf{x}, \mathbf{y}) : training data (2D inputs and 3D ground-truth outputs)
Require: F_ϕ : pose-net with parameters ϕ
Require: E_θ : loss-net with parameters θ
Require: optimizer_ϕ : optimizer for pose-net
Require: optimizer_θ : optimizer for loss-net
Require: T : number of training iterations
 1: Initialize ϕ_0, θ_0 randomly
 2: **for** $t = 1$ **to** T **do**
 3: Sample mini-batch $B_t = \{(x_i, y_i)\}_{i=1}^{|B_t|}$
 4: $\tilde{y}_i \leftarrow F_{\phi_{t-1}}(x_i)$ for all $(x_i, y_i) \in B_t$
 5: $g_\theta \leftarrow \nabla_{\theta} \frac{1}{|B_t|} \sum_{(x_i, y_i) \in B_t} L_E(x_i, y_i, \tilde{y}_i; \theta_{t-1})$
 6: $\theta_t \leftarrow \theta_{t-1} - \eta_\theta g_\theta$
 7: $g_\phi \leftarrow \nabla_{\phi} \frac{1}{|B_t|} \sum_{(x_i, y_i) \in B_t} L_F(x_i, y_i; \theta_t)$
 8: $\phi_t \leftarrow \phi_{t-1} - \eta_\phi g_\phi$
 9: **end for**

plausibility of predicted poses. The pose-net and loss-net are updated in an alternating manner, allowing the loss-net to adapt to the evolving predictions of the pose-net and provide informative structural learning signals. Specifically, the pose-net is optimized with a combined objective consisting of the standard mean squared error and the loss-net energy score, which we denote as \mathcal{L}_F , while the loss-net is trained with an energy-shaping objective \mathcal{L}_E that assigns lower energy to ground-truth poses and higher energy to implausible predictions. Although alternating updates can be unstable, we find that combining the energy term with supervised loss yields stable training and often faster convergence (§5.2).

Our framework can be seamlessly combined with various backbone models, from single-frame lifting models to multi-frame models, since the loss-net can be introduced independently of the pose-net architecture. Furthermore, it does not incur any additional inference cost because the loss-net is only used during training. The overall procedure is summarized in Algorithm 1, and detailed explanations are provided in Appendix A.1.

3.4. Graph-based Loss-Net.

In SEAL-pose, the capability of the loss-net to capture structural dependencies in the output space is crucial for guiding the pose-net toward more plausible predictions. Beyond merely modeling local (short-range) and global (long-range) relations, the loss-net must aggregate them into a unified, whole-pose signal that can effectively guide the task network. To further enhance this ability, we use a graph-based design for the loss-net, enabling more effective use of skeletal structure. We adopt Graphormer (Ying et al., 2021) as the loss-net backbone with task-specific simplifications, using self-attention to model both short- and long-range joint dependencies. This design results in a more expressive and structure-aware trainable loss function, providing stronger structural guidance for the task network and ultimately yielding more consistent and coherent 3D pose predictions.

In addition, to assess the suitability of graph-based structures, we also implement an MLP-based loss-net as a baseline. This comparison allows us to examine whether utilizing graph structure provides benefits over a simpler fully-connected neural network. Overall implementation details of loss-nets are provided in Appendix A.2.2.

3.5. Loss-net Input Design via Early Fusion

In 3D HPE, the output space is continuous, with infinitely many pose candidates. As a result, subtle differences in 2D cues and 3D hypotheses are often hard to disentangle in representation space when the two modalities are weakly coupled. Therefore, the energy should be conditioned on the 2D observation—ideally via early fusion—so that it reflects how compatible a 3D hypothesis is with the given evidence.

In contrast, SEAL was originally motivated by discrete structured prediction, where the loss-net typically operates on label embeddings. Its input design does not explicitly model 2D-conditioned 3D compatibility in geometric space. To better reflect this requirement in 3D HPE, we design a joint-aligned early-fusion input that directly exposes 2D–3D compatibility signals to the loss-net. Combined with a graph-based loss-net, early fusion captures fine-grained joint-wise 2D–3D compatibility, and message passing lifts these local cues to whole-skeleton consistency, producing globally coherent energies. Details are provided in Appendix A.7.

3.6. Negative Sampling Strategies

Because 3D poses lie in a continuous, high-dimensional space, negatives are effectively unbounded, which can make learning unstable. We therefore use a margin-based objective with hard negatives to provide a stable separation signal and enforce meaningful energy gaps.

Hard negatives from diffusion samples. A diffusion-based model generates multiple candidate poses per input. We construct a hard negative by selecting the candidate that best matches the 2D observation under reprojection:

$$\tilde{\mathbf{y}}_{\text{neg}} = \arg \min_{k=1, \dots, K} \text{MPJPE}_{2D} \left(\Pi \left(\tilde{\mathbf{y}}^{(k)} \right), \mathbf{u} \right),$$

where \mathbf{u} denotes the ground-truth 2D keypoints and $\Pi(\cdot)$ is the camera projection. This 2D-based selection yields a reprojection-consistent negative that better reflects 2D–3D compatibility.

Single-frame negatives from 2D perturbations. We construct K negative samples by perturbing the input 2D keypoints and passing them through the same deterministic pose-net:

$$x_{\text{noisy}}^{(k)} = x + \epsilon^{(k)}, \quad \epsilon^{(k)} \sim \mathcal{U}(\|\epsilon\|_2 \leq R_{\text{max}}), \quad (1)$$

$$\tilde{y}_{\text{neg}}^{(k)} = F_\phi \left(x_{\text{noisy}}^{(k)} \right), \quad k = 1, \dots, K. \quad (2)$$

We keep the original prediction-to-ground-truth margin loss and add a negative-negative ordering regularizer: we sort negatives by their 2D MPJPE and compare adjacent and randomly sampled pairs, encouraging the loss-net energy to capture fine-grained structural discrepancies.

$$\ell_{\text{pair}}(i, j) = \left[\kappa \text{MPJPE}(\tilde{y}_{\text{neg}}^{(i)}, \tilde{y}_{\text{neg}}^{(j)}) - E_{\text{neg}}^{(i)} + E_{\text{neg}}^{(j)} \right]_+ \quad (3)$$

Multi-frame extension via neighboring frames. In the multi-frame setting, we use the same pairwise loss, but leverage neighboring frames to form implicit negative pairs, using window-averaged poses and energies. We sample two nearby start indices t and s and form window-averaged pose and energy:

$$\bar{E}(u) = \frac{1}{w} \sum_{i=0}^{w-1} E_{u+i}, \quad \bar{y}(u) = \frac{1}{w} \sum_{i=0}^{w-1} \tilde{y}_{u+i}. \quad (4)$$

We then apply the same pairwise form:

$$\ell_{\text{pair}}(t, s) = \left[\kappa \cdot \text{MPJPE}(\bar{y}(t), \bar{y}(s)) - |\bar{E}(t) - \bar{E}(s)| \right]_+ \quad (5)$$

Detailed ablation results are reported in Appendix A.4.

4. Experimental Setup

4.1. Datasets and Evaluation Metrics

Datasets. We conduct our empirical experiments on Human3.6M dataset (H36M) (Ionescu et al., 2014), MPI-INF-3DHP (3DHP) (Mehta et al., 2017) dataset and Human3.6M 3D WholeBody dataset (H3WB) (Zhu et al., 2023). H36M is the most widely used dataset for 3D human pose estimation (Zheng et al., 2023; Liu et al., 2024). 3DHP is a more challenging dataset than H36M because it contains fewer samples and includes both indoor and outdoor scenes, while H36M only contains indoor scenes. H3WB is a recent dataset for 3D whole-body pose estimation. H3WB extends H36M by providing whole-body keypoint annotations with detailed information about hands, face, and feet, making it suitable for evaluating fine-grained 3D pose estimation. Following common practice on 3DHP, which is typically evaluated using ground-truth 2D inputs, we also report results on H36M with ground-truth 2D keypoints for a fair comparison across datasets.

Evaluation Metrics. We follow common practice in 3D human pose estimation and report standard metrics, such as mean per-joint position error (MPJPE), procrustes-aligned MPJPE (P-MPJPE), percentage of correct keypoints (PCK), area under curve (AUC), and pelvis-aligned MPJPE (PA-MPJPE), according to the evaluation protocol of each dataset. These metrics remain the standard benchmarks to evaluate per-joint error. However, they do not measure

structural plausibility, whether the predicted poses conform to anatomical constraints.

4.2. Structural Consistency Metrics

To further evaluate structural consistency, we introduce two additional metrics.

Limb Symmetry Error (LSE). LSE measures violation of the left-right symmetry by comparing the lengths of the corresponding limbs, such as the lower arms and thighs. For a limb pair $(\mathbf{l}_{i1}, \mathbf{l}_{i2}), (\mathbf{r}_{i1}, \mathbf{r}_{i2})$, LSE is defined as the normalized difference in length between the left and right counterparts:

$$\text{LSE}_i = 100 \cdot \left| \frac{\|\mathbf{l}_{i1} - \mathbf{l}_{i2}\| - \|\mathbf{r}_{i1} - \mathbf{r}_{i2}\|}{(\|\mathbf{l}_{i1} - \mathbf{l}_{i2}\| + \|\mathbf{r}_{i1} - \mathbf{r}_{i2}\|)/2} \right|$$

Body Segment Length Error (BSLE). BSLE measures deviations in the lengths of body segments, pair of adjacent joints, by comparing predicted poses and ground-truth poses. A special case of BSLE focuses on limbs, where symmetric differences are most pronounced, is referred to as **limb length error (LLE)**. For each segment i , with predicted adjacent keypoints $\mathbf{k}_{i1}, \mathbf{k}_{i2}$ and corresponding ground truth keypoints $\mathbf{t}_{i1}, \mathbf{t}_{i2}$, BSLE is defined as:

$$\text{BSLE}_i = 100 \cdot \left| 1 - \frac{\|\mathbf{k}_{i2} - \mathbf{k}_{i1}\|}{\|\mathbf{t}_{i2} - \mathbf{t}_{i1}\|} \right|$$

We emphasize that these metrics are not used as training loss. Instead, our trainable loss-net is designed to learn structural consistency directly from data without requiring explicit priors such as fixed bone lengths or symmetry constraints. LSE and BSLE are used solely for evaluation purposes, providing complementary insights into whether predicted poses are anatomically plausible.

4.3. Backbone models

We employed a diverse set of pose estimation models as our pose-net backbones, ranging from general baselines to recent state-of-the-art methods. Specifically, we used SimpleBaseline (Martinez et al., 2017), SemGCN (Zhao et al., 2019), and VideoPose (Pavlo et al., 2019) for single-frame setting, and MixSTE (Zhang et al., 2022), P-STMO (Shan et al., 2022), PoseFormerV2 (Zhao et al., 2023), D3DP (Shan et al., 2023), KTFformer (Peng et al., 2024) and MotionAGFormer (Mehraban et al., 2024) for multi-frame setting. These backbones cover a broad range of architectures, from commonly used designs to state-of-the-art models, allowing us to verify the effectiveness and robustness of SEAL-pose across different designs. Further implementation details are provided in the Appendix A.2.

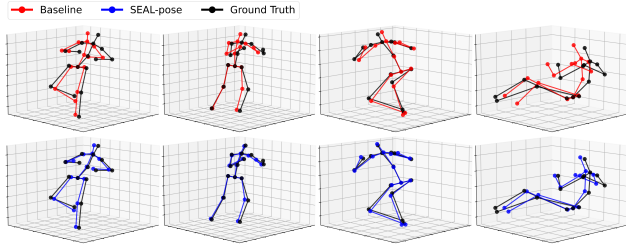


Figure 3. **Qualitative Comparison of Predicted Poses on H36M.** Predictions from SEAL-pose (bottom, blue) demonstrate clear improvements over the baseline (top, red) by producing structures closer to the ground-truth human pose (black).

5. Experimental Results

We provide a comprehensive set of 34 experimental results (single-frame models: 3 baselines \times 3 datasets \times 2 SEAL-pose variants; multi-frame models: 4 baselines \times 2 variants on H36M and 3DHP), which consistently corroborate our findings and offer strong evidence for the robustness and generalizability of our approach.

5.1. Comparison with Baselines

Single-Frame Settings. As shown in Table 1 (Human3.6M) and Table 2 (MPI-INF-3DHP), SEAL-pose consistently improves performance across all baseline models. On Human3.6M, SEAL-pose reduces both MPJPE and P-MPJPE, with graph-based loss-net variants yielding the largest gains. On MPI-INF-3DHP, which contains more diverse and In-The-Wild scenarios, the improvements are even more pronounced. SEAL-pose also improves whole-body pose estimation on the H3WB dataset, as shown in (Table 3), demonstrating that our trainable loss function is also beneficial in complex whole-body settings. However, when the loss-net is graph-based, its bias toward local neighborhoods may underutilize global context and thus underperform a simpler MLP loss-net. We leave a deeper analysis of the balance between local and global reasoning for future work.

Multi-Frame Settings. Multi-frame models already perform strongly by leveraging temporal information, and recent architectures have largely reached a saturated regime in benchmark performance. In this work, we apply SEAL-pose to a broad set of multi-frame backbones, including general transformer-style baselines (P-STMO, MixSTE, PoseFormerV2), a diffusion-based model (D3DP), and recent state-of-the-art methods (KTPFormer, MotionAGFormer). Despite the strength of these models, adding our loss-net consistently yields additional improvements across all backbones, as shown in Table 1 and Table 2.

5.2. Training stability and hyperparameter search

The convergence trends in Fig. 7 further support stable optimization. We retain an explicit supervised regression loss

in \mathcal{L}_F as an optimization anchor, and use the energy term only as an auxiliary regularizer that shapes structural plausibility; this anchor stabilizes training and yields reliable convergence.

Building on this stability, rather than exhaustively searching the large hyperparameter space, we adopt a simple greedy tuning protocol (Appendix A.5), which is efficient in practice. To further verify robustness, we additionally evaluate several nearby sub-optimal settings; Table 8 and Fig. 8 show consistent convergence behavior without instability.

5.3. Structural Consistency Evaluation

We evaluated structural consistency by examining the LSE, LLE, and BSLE metrics on the H36M, 3DHP, and H3WB datasets. For comparison, we also included a setting with explicit bone length constraints as a loss term, to directly contrast SEAL-pose with manually designed constraint-based approaches.

In result, SEAL-pose consistently showed lower error values across all three structural metrics on H36M and 3DHP datasets, as detailed in Table 4. These results indicate that SEAL-pose effectively captures structured dependencies in human poses, leading to more anatomically plausible and consistent 3D pose predictions. For a more detailed examination, we grouped samples into bins with comparable P-MPJPE and analyzed our proposed structural consistency metrics (LSE, BSLE, LLE) within each bin. Even when comparing predictions with similar P-MPJPE, SEAL-pose consistently yielded lower values on these metrics than the baseline, as shown in Fig. 4. These intra-bin comparisons reveal a limitation of standard training objective: by optimizing primarily for pointwise coordinate error (e.g. MSE, MPJPE), they are relatively insensitive to violations of structural plausibility (e.g., symmetry, limb proportionality, kinematic consistency), leading to higher LSE/BSLE/LLE within similar P-MPJPE ranges. Notably, LSE is defined without reference to ground truth, yet the results on 3DHP highlight that SEAL-pose more effectively internalizes structural constraints. On Human3.6M, absolute errors are already small, so the differences are less pronounced, but SEAL-pose still demonstrates an advantage over the baseline.

However, SEAL-pose showed mixed results on the H3WB dataset, This is likely due to the dataset’s noisy labeling, which is shown from the relatively high LSE of the ground truth poses. Moreover, since H3WB provides annotations for a very large number of keypoints including body, face, hands, and feet, capturing coherent structural dependencies across all regions is inherently more challenging, making further improvements less straightforward. While SEAL-pose did not significantly outperform the baseline in this setting, it still achieved better results compared to directly

Table 1. Performances on Human3.6M. SEAL-pose improves MPJPE and P-MPJPE across models. D3DP and KTPformer use $T=243$, $H=20$, $K=10$, J_{Best} .

Method	MPJPE↓	P-MPJPE↓
<i>Single-frame models</i>		
SimpleBaseline (Martinez et al., 2017)	43.8	34.7
+ SEAL-pose (MLP)	42.5	33.9
+ SEAL-pose (Graph)	40.7	32.3
SemGCN (Zhao et al., 2019)	47.0	37.9
+ SEAL-pose (MLP)	44.9	36.5
+ SEAL-pose (Graph)	43.4	35.7
VideoPose (Pavlo et al., 2019)	41.6	32.4
+ SEAL-pose (MLP)	41.0	32.3
+ SEAL-pose (Graph)	41.2	32.1
Method	MPJPE↓	P-MPJPE↓
<i>Multi-frame models</i>		
MixSTE ($T=243$) (Zhang et al., 2022)	20.8	16.1
+ SEAL-pose (MLP)	20.6	15.8
+ SEAL-pose (Graph)	20.0	15.7
Poseformer V2 ($T=27$) (Zhao et al., 2023)	42.7	31.6
+ SEAL-pose (MLP)	41.5	31.2
+ SEAL-pose (Graph)	40.5	30.3
D3DP (Shan et al., 2023)	20.4	15.4
+ SEAL-pose (MLP)	18.1	13.9
+ SEAL-pose (Graph)	17.7	13.7
KTPformer (Peng et al., 2024)	18.9	14.3
+ SEAL-pose (MLP)	18.9	14.5
+ SEAL-pose (Graph)	18.3	13.9

Table 3. Performance on the Human3.6M WholeBody. SEAL-pose reduces P-MPJPE across all body parts, resulting in more coherent predictions. † from H3WB’s official benchmark. ‡ nose-aligned MPJPE for face and wrist-aligned MPJPE for hands.

Method	Whole-body	Body	Face/Aligned [†]	Hand/Aligned [‡]
Jointformer [†]	88.3	84.9	66.5 / 17.8	125.3 / 43.7
3D-LFM	64.1	60.8	56.6 / 10.4	78.2 / 28.2
SimpleBaseline (Martinez et al., 2017)	67.4	63.3	49.9 / 14.1	98.0 / 34.8
+ SEAL-pose (MLP)	62.8	61.1	46.3 / 13.7	90.7 / 34.2
+ SEAL-pose (Graph)	64.8	61.6	47.6 / 13.3	94.0 / 34.5
VideoPose (Pavlo et al., 2019)	61.5	57.4	48.8 / 11.9	84.1 / 30.3
+ SEAL-pose (MLP)	58.6	54.8	45.0 / 11.5	82.3 / 29.3
+ SEAL-pose (Graph)	59.5	56.3	46.1 / 11.5	82.3 / 28.7

injecting explicit structural constraints, suggesting that a trainable loss function provides a more flexible and generalizable way of enforcing plausibility in whole-body pose estimation. Overall, the improved structural consistency metrics highlight that loss-net’s ability to capture structures in human poses helps the pose-net to predict more anatomically consistent and plausible 3D human poses.

5.4. Ablation Studies

Analysis of the Energy-Guided Pose-Net. We conduct gradient-based inference (GBI) on the output of the pose-net using the trained loss-net to verify its ability to capture plausible human pose structures. Starting from the pose-net prediction, GBI iteratively refines the pose by following

Table 2. Performances on MPI-INF-3DHP. SEAL-pose consistently reduces MPJPE and improves PCK and AUC. D3DP uses $T=243$, $H=20$, $K=20$, J_{Best} .

Method	MPJPE↓	PCK↑	AUC↑
<i>Single-frame models</i>			
SimpleBaseline (Martinez et al., 2017)	80.9	86.9	53.8
+ SEAL-pose (MLP)	71.8	89.3	58.7
+ SEAL-pose (Graph)	68.2	90.2	60.4
SemGCN (Zhao et al., 2019)	74.5	89.5	56.4
+ SEAL-pose (MLP)	71.8	90.4	57.9
+ SEAL-pose (Graph)	62.9	92.7	61.7
VideoPose (Pavlo et al., 2019)	66.4	90.8	60.5
+ SEAL-pose (MLP)	64.0	91.7	62.1
+ SEAL-pose (Graph)	62.2	91.8	63.1
Method	MPJPE↓	PCK↑	AUC↑
<i>Multi-frame models</i>			
P-STMO ($T=81$) (Shan et al., 2022)	33.4	98.0	77.5
+ SEAL-pose (MLP)	32.9	98.1	77.7
+ SEAL-pose (Graph)	32.5	98.2	78.0
Poseformer V2 ($T=27$) (Zhao et al., 2023)	29.6	97.0	77.8
+ SEAL-pose (MLP)	28.5	97.4	78.4
+ SEAL-pose (Graph)	27.8	97.5	79.0
D3DP (Shan et al., 2023)	28.8	98.2	80.4
+ SEAL-pose (MLP)	28.5	98.6	80.8
+ SEAL-pose (Graph)	27.8	98.7	80.9
MotionAGFormer-L (Mehraban et al., 2024)	16.2	98.2	85.3
+ SEAL-pose (MLP)	15.2	99.1	89.0
+ SEAL-pose (Graph)	15.3	99.0	88.9

Table 4. Structural Consistency Evaluation Across Datasets. SEAL-pose reduces structural error metrics such as LSE, LLE, and BSLE (see §4.2 for the definitions), improving plausibility.

Dataset	Metric	MPJPE↓	LSE↓	LLE↓	BSLE↓
H36M	Ground Truth		0.00	0.00	0.00
	SimpleBaseline (Martinez et al., 2017)	43.8	4.85	5.09	6.12
	+ Constraint (Cao & Zhao, 2021)	41.5	4.35	4.54	6.17
	+ SEAL-pose	40.7	3.68	3.94	5.49
3DHP	Ground Truth		1.21	0.00	0.00
	SimpleBaseline (Martinez et al., 2017)	80.9	10.14	11.60	8.13
	+ Constraint (Cao & Zhao, 2021)	75.0	7.80	10.02	7.87
	+ SEAL-pose	68.2	6.22	6.02	5.93
H3WB	Ground Truth		4.42	0.00	0.00
	SimpleBaseline (Martinez et al., 2017)	67.4	6.60	6.56	6.22
	+ Constraint (Cao & Zhao, 2021)	65.1	6.88	6.82	6.66
	+ SEAL-pose	62.8	6.55	6.13	6.73

gradient signals from the loss-net, which are expected to lower the assigned energy (Appendix A.3). Each iteration corresponds to a single training-style update step, and the curves—averaged over all test examples—show gradual improvement rather than drastic one-step changes. Since these metrics directly reflect structural plausibility, the consistent reduction indicates that the loss-net effectively captures human pose structure and provides meaningful gradient signals. The effect is more pronounced on the challenging 3DHP dataset, but the same trend is also observed on H36M, as shown in Fig. 6 in Appendix A.3, confirming the consistency of the results.

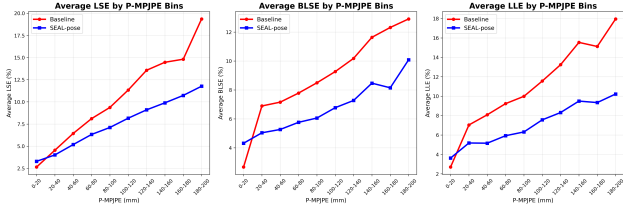


Figure 4. Comparison of structural consistency in MPI-INF-3DHP. Average structural inconsistency measures (from left to right: LSE, BSLE, LLE) are displayed for predictions of baselines (red) and SEAL-pose (blue) binned by P-MPJPE. SEAL-pose consistently achieves lower structural errors even under similar P-MPJPEs.

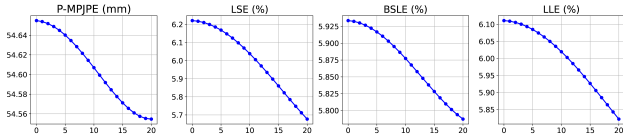


Figure 5. Gradient-Based Inference results on MPI-INF-3DHP. P-MPJPE, LSE, LLE, and BSLE all decrease steadily over iterations, indicating that the loss-net effectively captures structural plausibility and provides meaningful corrective feedback to the pose-net.

Analysis of the Learned Energy. We further examine whether the loss-net energy aligns with structural consistency metrics. The graph-based loss-net energy exhibits a positive correlation with the proposed structural metrics (LSE/BSLE/LLE), implying that higher energy corresponds to less structurally plausible poses. For instance, for LSE we observe Kendall’s $\tau \approx 0.29$, which corresponds to roughly 65% correct pairwise orderings. For the other metrics, we obtain 59.1% for BSLE and 60.6% for LLE. This suggests that the energy correlates with global structural plausibility, especially symmetry consistency.

Analysis of Graph-based Architecture. We compared graph-based and MLP-based loss-nets. Overall results show that the graph-based loss-net consistently provides better structural guidance, leading to lower per-joint errors and improved structural plausibility, as shown in Sections 5.1 and 5.3. This trend is also reflected in the pairwise ordering analysis: the graph-based loss-net achieves $\sim 10\%$ higher correct pairwise orderings than the MLP-based loss-net across our structural metrics. This suggests that the graph-based loss-net provides more suitable training signals for learning structure-aware guidance.

Cross-Dataset Evaluation for Generalization and Robustness To test whether the loss-net overfits the training data, we run cross-dataset experiments between Human3.6M (H36M) and MPI-INF-3DHP (3DHP), training on one dataset and evaluating on the other. If the loss-net were merely memorizing domain-specific patterns, adding SEAL-pose would be expected to worsen cross-dataset performance relative to the baseline, which would provide di-

rect evidence of overfitting. These results highlight two key points. First, the cross-dataset experiments indicate that limited domain generalization and sensitivity to input formatting are common issues in 3D HPE models, as both the baseline and SEAL-pose suffer from dataset shift. Second, regarding the original concern about the overfitting of the loss-net, we actually observe the opposite behavior as the gain of SEAL-pose over the baseline increases under the domain shift (Fig. 11, Table 5). This suggests that the loss-net does not overfit in a way that harms the pose-net’s cross-dataset performance. Finally, we complement the cross-dataset evaluation with qualitative results on In-The-Wild images to further assess robustness. As shown in Appendix A.6 (Fig. 9, 10), SEAL-pose yields more structurally consistent poses than the baseline (PoseFormerV2, KTPFormer) on the In-The-Wild images.

Table 5. Cross-dataset evaluation between Human3.6M (H36M) and MPI-INF-3DHP (3DHP) using PoseFormerV2. SEAL-pose does not introduce additional degradation beyond the baseline under dataset shift, suggesting no harmful loss-net overfitting.

Train \rightarrow Test	MPJPE \downarrow		P-MPJPE \downarrow	
	Baseline	SEAL-pose	Baseline	SEAL-pose
H36M \rightarrow 3DHP	111.4	97.3	83.2	70.3
3DHP \rightarrow H36M	157.0	151.9	109.7	107.9

6. Conclusion

In this paper, we propose SEAL-pose, a novel framework that introduces a trainable loss function for 3D human pose estimation. Unlike prior approaches relying on explicit priors or architecture-specific constraints, our proposed loss-net learns structural dependencies directly from data, and can be seamlessly integrated with a wide range of backbone pose-nets. We design the loss-net as a graph-based model, representing joints as nodes and bones as edges, which enables principled learning of both local (bone lengths, adjacency) and global (symmetry, long-range relations) dependencies in human pose. Our experiments on Human3.6M, MPI-INF-3DHP, and H3WB demonstrate that SEAL-pose not only reduces per-joint pose estimation errors, but also improves structural plausibility, confirmed by our proposed LSE and BSLE metrics, showing that the graph-based loss-net provides stronger structural guidance. Overall, SEAL-pose highlights the promise of trainable loss functions as a general paradigm for structured prediction tasks with complex output dependencies.

7. Impact Statements

This paper proposes SEAL-pose, a trainable loss-function framework for 3D human pose estimation that learns structural dependencies among joints directly from data. By training a pose-net using a loss-net that evaluates structural plausibility, SEAL-pose reduces per-joint errors while improving the overall structural validity of predicted poses. This can enable more reliable pose estimation for downstream applications such as motion analysis, human-computer interaction, sports analytics, rehabilitation/healthcare, and animation.

As with human-centric perception models in general, the proposed approach could be misused for privacy-invasive purposes such as surveillance or tracking, and dataset biases may lead to performance disparities under certain environments or conditions. Future work should strengthen robustness evaluation across diverse datasets and in-the-wild settings, and deployment should follow consent-based and privacy-preserving principles.

References

- Belanger, D. and McCallum, A. Structured prediction energy networks. In Balcan, M. and Weinberger, K. Q. (eds.), *Proceedings of the 33rd International Conference on Machine Learning, ICML 2016, New York City, NY, USA, June 19-24, 2016*, volume 48 of *JMLR Workshop and Conference Proceedings*, pp. 983–992. JMLR.org, 2016. URL <http://proceedings.mlr.press/v48/belanger16.html>.
- Bigalke, A., Hansen, L., Diesel, J., and Heinrich, M. P. Domain adaptation through anatomical constraints for 3d human pose estimation under the cover. In Konukoglu, E., Menze, B., Venkataraman, A., Baumgartner, C., Dou, Q., and Albarqouni, S. (eds.), *Proceedings of The 5th International Conference on Medical Imaging with Deep Learning*, volume 172 of *Proceedings of Machine Learning Research*, pp. 173–187. PMLR, 06–08 Jul 2022. URL <https://proceedings.mlr.press/v172/bigalke22a.html>.
- Cao, X. and Zhao, X. Anatomy and geometry constrained one-stage framework for 3d human pose estimation. In Ishikawa, H., Liu, C.-L., Pajdla, T., and Shi, J. (eds.), *Computer Vision – ACCV 2020*, pp. 227–243, Cham, 2021. Springer International Publishing. ISBN 978-3-030-69525-5.
- Chen, T., Fang, C., Shen, X., Zhu, Y., Chen, Z., and Luo, J. Anatomy-aware 3d human pose estimation with bone-based pose decomposition. *IEEE Trans. Cir. and Sys. for Video Technol.*, 32(1):198–209, January 2022. ISSN 1051-8215. doi: 10.1109/TCSVT.2021.3057267. URL <https://doi.org/10.1109/TCSVT.2021.3057267>.
- Fang, H., Xu, Y., Wang, W., Liu, X., and Zhu, S. Learning pose grammar to encode human body configuration for 3d pose estimation. In McIlraith, S. A. and Weinberger, K. Q. (eds.), *Proceedings of the Thirty-Second AAAI Conference on Artificial Intelligence, (AAAI-18), the 30th Innovative Applications of Artificial Intelligence (IAAI-18), and the 8th AAAI Symposium on Educational Advances in Artificial Intelligence (EAAI-18), New Orleans, Louisiana, USA, February 2-7, 2018*, pp. 6821–6828. AAAI Press, 2018. doi: 10.1609/AAAI.V32I1.12270. URL <https://doi.org/10.1609/aaai.v32i1.12270>.
- Gatys, L. A., Ecker, A. S., and Bethge, M. Texture synthesis using convolutional neural networks. In Cortes, C., Lawrence, N. D., Lee, D. D., Sugiyama, M., and Garnett, R. (eds.), *Advances in Neural Information Processing Systems 28: Annual Conference on Neural Information Processing Systems 2015, December 7-12, 2015, Montreal, Quebec, Canada*, pp. 262–270, 2015a. URL <https://proceedings.neurips.cc/paper/2015/hash/a5e00132373a7031000fd987a3c9f87b-Abstract.html>.
- Gatys, L. A., Ecker, A. S., and Bethge, M. A neural algorithm of artistic style. *CoRR*, abs/1508.06576, 2015b. URL <http://arxiv.org/abs/1508.06576>.
- Goodfellow, I. J., Shlens, J., and Szegedy, C. Explaining and harnessing adversarial examples. In Bengio, Y. and LeCun, Y. (eds.), *3rd International Conference on Learning Representations, ICLR 2015, San Diego, CA, USA, May 7-9, 2015, Conference Track Proceedings*, 2015. URL <http://arxiv.org/abs/1412.6572>.
- Ionescu, C., Papava, D., Olaru, V., and Sminchisescu, C. Human3.6m: Large scale datasets and predictive methods for 3d human sensing in natural environments. *IEEE Transactions on Pattern Analysis and Machine Intelligence*, 2014.
- Kim, J.-H. and Lee, S.-W. Toward approaches to scalability in 3d human pose estimation. In *The Thirty-eighth Annual Conference on Neural Information Processing Systems*, 2024. URL <https://openreview.net/forum?id=xse8QMGnyM>.
- Kingma, D. P. and Ba, J. Adam: A method for stochastic optimization. In Bengio, Y. and LeCun, Y. (eds.), *3rd International Conference on Learning Representations, ICLR 2015, San Diego, CA, USA, May 7-9, 2015, Conference Track Proceedings*, 2015. URL <http://arxiv.org/abs/1412.6980>.

- Kipf, T. N. and Welling, M. Semi-supervised classification with graph convolutional networks. In *International Conference on Learning Representations*, 2017. URL <https://openreview.net/forum?id=SJU4ayYgl>.
- Lee, J. Y., Mehta, S. V., Wick, M. L., Tristan, J., and Carbonell, J. G. Gradient-based inference for networks with output constraints. In *The Thirty-Third AAAI Conference on Artificial Intelligence, AAAI 2019, The Thirty-First Innovative Applications of Artificial Intelligence Conference, IAAI 2019, The Ninth AAAI Symposium on Educational Advances in Artificial Intelligence, EAAI 2019, Honolulu, Hawaii, USA, January 27 - February 1, 2019*, pp. 4147–4154. AAAI Press, 2019. doi: 10.1609/AAAI.V33I01.33014147. URL <https://doi.org/10.1609/aaai.v33i01.33014147>.
- Lee, J.-Y., Patel, D., Goyal, P., Zhao, W., Xu, Z., and McCollum, A. Structured energy network as a loss. In Oh, A. H., Agarwal, A., Belgrave, D., and Cho, K. (eds.), *Advances in Neural Information Processing Systems*, 2022. URL https://openreview.net/forum?id=F0DowhX7_x.
- Liu, Y., Qiu, C., and Zhang, Z. Deep learning for 3d human pose estimation and mesh recovery: A survey. *Neurocomputing*, pp. 128049, 2024. ISSN 0925-2312. doi: <https://doi.org/10.1016/j.neucom.2024.128049>.
- Ma, Z. and Collins, M. Noise contrastive estimation and negative sampling for conditional models: Consistency and statistical efficiency. In Riloff, E., Chiang, D., Hockenmaier, J., and Tsujii, J. (eds.), *Proceedings of the 2018 Conference on Empirical Methods in Natural Language Processing*, pp. 3698–3707, Brussels, Belgium, October-November 2018. Association for Computational Linguistics. doi: 10.18653/v1/D18-1405. URL <https://aclanthology.org/D18-1405/>.
- Martinez, J., Hossain, R., Romero, J., and Little, J. J. A simple yet effective baseline for 3d human pose estimation. In *2017 IEEE International Conference on Computer Vision (ICCV)*, pp. 2659–2668, 2017. doi: 10.1109/ICCV.2017.288.
- Mehraban, S., Adeli, V., and Taati, B. Motionagformer: Enhancing 3d human pose estimation with a transformer-gcnformer network. In *Proceedings of the IEEE/CVF Winter Conference on Applications of Computer Vision (WACV)*, pp. 6920–6930, January 2024.
- Mehta, D., Rhodin, H., Casas, D., Fua, P., Sotnychenko, O., Xu, W., and Theobalt, C. Monocular 3d human pose estimation in the wild using improved cnn supervision. In *2017 International Conference on 3D Vision (3DV)*, pp. 506–516, 2017. doi: 10.1109/3DV.2017.00064.
- Mordvintsev, A., Olah, C., and Tyka, M. Inceptionism: Going deeper into neural networks, 2015. URL <https://api.semanticscholar.org/CorpusID:69951972>.
- Pavlakos, G., Zhou, X., Derpanis, K. G., and Daniilidis, K. Coarse-to-fine volumetric prediction for single-image 3D human pose. In *Computer Vision and Pattern Recognition (CVPR)*, 2017.
- Pavlakos, G., Zhou, X., and Daniilidis, K. Ordinal depth supervision for 3D human pose estimation. In *Computer Vision and Pattern Recognition (CVPR)*, 2018.
- Pavlo, D., Feichtenhofer, C., Grangier, D., and Auli, M. 3d human pose estimation in video with temporal convolutions and semi-supervised training. In *Conference on Computer Vision and Pattern Recognition (CVPR)*, 2019.
- Peng, J., Zhou, Y., and Mok, P. Ktpformer: Kinematics and trajectory prior knowledge-enhanced transformer for 3d human pose estimation. In *Proceedings of the IEEE/CVF Conference on Computer Vision and Pattern Recognition*, pp. 1123–1132, 2024.
- Rommel, C., Letzelter, V., Samet, N., Marlet, R., Cord, M., Pérez, P., and Valle, E. Manipose: Manifold-constrained multi-hypothesis 3d human pose estimation. In *Advances in Neural Information Processing Systems*, volume 37. Curran Associates, Inc., 2024.
- Shan, W., Liu, Z., Zhang, X., Wang, S., Ma, S., and Gao, W. P-stmo: Pre-trained spatial temporal many-to-one model for 3d human pose estimation. In *Computer Vision—ECCV 2022: 17th European Conference, Tel Aviv, Israel, October 23–27, 2022, Proceedings, Part V*, pp. 461–478. Springer, 2022.
- Shan, W., Liu, Z., Zhang, X., Wang, Z., Han, K., Wang, S., Ma, S., and Gao, W. Diffusion-based 3d human pose estimation with multi-hypothesis aggregation. In *Proceedings of the IEEE/CVF International Conference on Computer Vision*, pp. 14761–14771, 2023.
- Vaswani, A., Shazeer, N., Parmar, N., Uszkoreit, J., Jones, L., Gomez, A. N., Kaiser, L., and Polosukhin, I. Attention is all you need, 2023. URL <https://arxiv.org/abs/1706.03762>.
- Veličković, P., Cucurull, G., Casanova, A., Romero, A., Liò, P., and Bengio, Y. Graph attention networks. In *International Conference on Learning Representations*, 2018. URL <https://openreview.net/forum?id=rJXMpikCZ>.
- Wu, L., Yu, Z., Liu, Y., and Liu, Q. Limb pose aware networks for monocular 3d pose estimation. *IEEE Transactions on Image Processing*, 31:906–917, 2022. doi: 10.1109/TIP.2021.3136613.

- Xu, Y., Wang, W., Liu, T., Liu, X., Xie, J., and Zhu, S. Monocular 3d pose estimation via pose grammar and data augmentation. *IEEE Trans. Pattern Anal. Mach. Intell.*, 44(10):6327–6344, 2022. doi: 10.1109/TPAMI.2021.3087695. URL <https://doi.org/10.1109/TPAMI.2021.3087695>.
- Ying, C., Cai, T., Luo, S., Zheng, S., Ke, G., He, D., Shen, Y., and Liu, T.-Y. Do transformers really perform badly for graph representation? *Advances in neural information processing systems*, 34:28877–28888, 2021.
- Zhang, J., Tu, Z., Yang, J., Chen, Y., and Yuan, J. Mixste: Seq2seq mixed spatio-temporal encoder for 3d human pose estimation in video. In *Proceedings of the IEEE/CVF Conference on Computer Vision and Pattern Recognition (CVPR)*, pp. 13232–13242, June 2022.
- Zhao, L., Peng, X., Tian, Y., Kapadia, M., and Metaxas, D. N. Semantic graph convolutional networks for 3d human pose regression. In *IEEE Conference on Computer Vision and Pattern Recognition (CVPR)*, pp. 3425–3435, 2019.
- Zhao, Q., Zheng, C., Liu, M., Wang, P., and Chen, C. Poseformerv2: Exploring frequency domain for efficient and robust 3d human pose estimation. In *Proceedings of the IEEE/CVF Conference on Computer Vision and Pattern Recognition (CVPR)*, pp. 8877–8886, June 2023.
- Zhao, W., Wang, W., and Tian, Y. Graformer: Graph-oriented transformer for 3d pose estimation. In *Proceedings of the IEEE/CVF Conference on Computer Vision and Pattern Recognition (CVPR)*, pp. 20438–20447, June 2022.
- Zheng, C., Zhu, S., Mendieta, M., Yang, T., Chen, C., and Ding, Z. 3d human pose estimation with spatial and temporal transformers. *Proceedings of the IEEE International Conference on Computer Vision (ICCV)*, 2021.
- Zheng, C., Wu, W., Chen, C., Yang, T., Zhu, S., Shen, J., Kehtarnavaz, N., and Shah, M. Deep learning-based human pose estimation: A survey. *ACM Comput. Surv.*, 56(1), aug 2023. ISSN 0360-0300. doi: 10.1145/3603618. URL <https://doi.org/10.1145/3603618>.
- Zheng, X., Chen, X., and Lu, X. A joint relationship aware neural network for single-image 3d human pose estimation. *IEEE Transactions on Image Processing*, 29:4747–4758, 2020. doi: 10.1109/TIP.2020.2972104.
- Zhu, Y., Samet, N., and Picard, D. H3wb: Human3.6m 3d wholebody dataset and benchmark. In *Proceedings of the IEEE/CVF International Conference on Computer Vision (ICCV)*, pp. 20166–20177, October 2023.

A. Appendix

A.1. Detailed SEAL-pose

In our framework, the pose-net $F_\phi(x)$ is optimized to minimize a weighted sum of the mean squared error (MSE) loss and the output of the loss-net (energy) $E_\theta(x, \tilde{y})$. Specifically, the pose-net parameters ϕ are updated in the following manner:

$$\phi_t \leftarrow \phi_{t-1} - \eta_\phi \nabla_\phi \frac{1}{|B_t|} \sum_{(x,y) \in B_t} L_F(\phi; \theta), \quad (6)$$

where B_t is the mini-batch of training samples at iteration t , η_ϕ is the learning rate for the pose-net, and $L_F(\phi; \theta)$ is the combined loss function. The combined loss function is defined as:

$$L_F(x_i, y_i; \theta) = \sum_{j=1}^M \text{MSE}(y_j, F_\phi(x)_j) + \alpha E_\theta(x, F_\phi(x)), \quad (7)$$

where M refers to the total number of joints in the pose estimation dataset and x represents the input data, specifically the 2D joint coordinates. The variable y_j denotes the ground-truth 3D joint coordinates, while $F_\phi(x)_j = \tilde{y}_j$ represents the predicted 3D joint coordinates from the pose-net. The energy term $E_\theta(x, F_\phi(x))$ is computed by the loss-net and implicitly evaluates the structural dependencies between joints. Finally, α is a hyperparameter controlling the balance between the MSE loss and the energy term.

The loss-net is dynamically trained to adapt to the pose-net’s predictions by minimizing the loss L_E :

$$\theta_t \leftarrow \theta_{t-1} - \eta_\theta \nabla_\theta \frac{1}{|B_t|} \sum_{(x,y) \in B_t} L_E(x, y, F_{\phi_{t-1}}(x); \theta). \quad (8)$$

We employ two types of loss for L_E : margin-based loss and a simplified form of noise contrastive estimation (NCE) ranking loss (Ma & Collins, 2018), both suggested in (Lee et al., 2022).

The margin-based loss enforces the loss-net to decrease the energy $E_\theta(x, y)$ of the ground truth label y and increase the energy $E_\theta(x, \tilde{y})$ of the pose-net’s incorrect prediction \tilde{y} , such that the difference between the two energies is sufficiently large to exceed the margin. The margin-based loss is defined as:

$$L_E^{\text{margin}}(x_i, y_i, \tilde{y}_i; \theta) = \max_{\tilde{y}} [\Delta(y, \tilde{y}) - E_\theta(x, \tilde{y}) + E_\theta(x, y)]_+, \quad (9)$$

where $\Delta(y, \tilde{y})$ denotes a task-specific margin function, MPJPE in our implementation.

Similarly, the NCE ranking loss minimizes the energy of the ground truth label y while increasing the energy of the

pose-net’s prediction \tilde{y} , treating the pose-net’s predictions as negative samples. The NCE ranking loss is defined as:

$$L_E^{\text{NCE}}(x_i, y_i, \tilde{y}_i; \theta) = -\log \frac{\exp(-E_\theta(x, y))}{\exp(-E_\theta(x, y)) + \exp(-E_\theta(x, \tilde{y}))}. \quad (10)$$

A.2. Implementation Details

A.2.1. POSE-NET

We have modified the input and output layers of pose-net models to align with the dimensions of each dataset. In single-frame settings, we used separate Adam optimizers (Kingma & Ba, 2015) without learning rate decay for the loss-net and pose-net and trained models with a batch size of 1024 for 50 epochs on H36M and 3DHP, and a batch size of 64 for 200 epochs on H3WB. For multi-frame backbones, we adopt the training configurations from the original works—i.e., the same training schedules, data augmentations, and hyperparameters as in their papers/official implementations. In our experiments, we do not retune backbone-specific settings; instead, we only vary three hyperparameters introduced by our method: the pose-net learning rate (lr_p), the loss-net learning rate (lr_l), and the energy weight (α).

A.2.2. LOSS-NET

Graphormer injects structure into self-attention by adding shortest path distance (SPD)–based spatial bias $b_{\phi(v_i, v_j)}$ and an edge-path bias c_{ij} (edges along a shortest path) to the attention logits:

$$A_{ij} = \frac{(h_i W_Q)(h_j W_K)^\top}{\sqrt{d}} + b_{\phi(v_i, v_j)} + c_{ij}.$$

Separately, degree-based centrality is encoded by adding learnable embeddings to node inputs (not as an attention bias) (Ying et al., 2021). Because human skeletal graphs are small and regular compared with molecular or social networks, we adopt Graphormer’s core idea while simplifying it for human pose estimation. Concretely, we (i) remove node-level degree–centrality embeddings and (ii) do not define categorical edge types. On small, skeletal graphs, such handcrafted encodings can act like noise and distract attention, so we eliminate them and let the model infer structure directly from data while retaining only the shortest-path biases. This minimalist biasing reduces spurious inductive signals and helps the pose-net produce outputs with stronger structural consistency. Beyond encoding local and global dependencies, Graphormer also introduces a global, CLS-like virtual node v_{cls} that aggregates whole-graph information (Ying et al., 2021). We adopt this component in the loss-net: a virtual node v_{cls} attends to all joints and produces a compact summary signal of skeletal structure.

This design summarizes pose-level structure and guides the pose-net toward structurally coherent outputs.

We design the graph-based loss-net, following the Graphormer foundation, with model width $d=256$, $H=8$ attention heads, depth = 6 blocks; the same graph bias is shared across layers. For inputs, we represent each node by concatenating the keypoint’s 2D coordinates with its predicted 3D coordinates and encoding the joint identity via a one-hot vector; the resulting feature is linearly projected to dimension $d=32$, and a learnable CLS token is prepended. The head is an MLP that outputs a scalar energy, and we train the loss-net with either a margin-based objective (e.g., an MPJPE margin) or NCE.

For the MLP loss-net, we adjusted the SimpleBaseline architecture by modifying the dimensions and depth of the hidden layers. Specifically, we set the hidden size to 2048 with 2 residual block stages and omitted batch normalization and dropout layers.

A.3. Gradient-Based Inference

We implement a gradient-based inference (GBI) method with trained loss-net and pose-net, to examine whether the loss-net effectively captures structural dependencies in human poses. GBI is a method that leverages gradients to iteratively refine the outputs (Goodfellow et al., 2015; Mordvintsev et al., 2015; Gatys et al., 2015b;a; Belanger & McCallum, 2016) or parameters (Lee et al., 2019) of neural networks, and we adopt the former approach. Specifically, we iteratively update the predictions of pose-net along the gradient provided by the loss-net, with the objective of decreasing the energy. This procedure provides a direct way to evaluate whether the learned energy function captures human pose structure. If the loss-net has successfully learned structural dependencies, then following its gradient should progressively refine the predictions toward more plausible poses. The results on the H36M dataset are shown in Fig. 6, where all metrics steadily decrease over iterations, consistent with the trends observed for 3DHP in Fig. 5.

A.4. Result of Negative Sampling Strategies

In diffusion-based models, selecting the lowest-MPJPE sample as a hard negative yields the largest gain for multi-frame models, reducing MPJPE by 2.7mm on H36M. In the single-frame setting, we generate synthetic negatives by perturbing 2D keypoints and forwarding them through the same deterministic pose-net. On 3DHP (MPJPE), the proposed negative-negative pairwise regularizer (Sec. 3.6) provides additional gains of 2.6mm for SimpleBaseline and 0.6mm for SemGCN (Table 6), while VideoPose shows no noticeable change. Finally, in the multi-frame setting, we further introduce a neighboring-window negative term that contrasts hypotheses across nearby frames; this yields a modest but

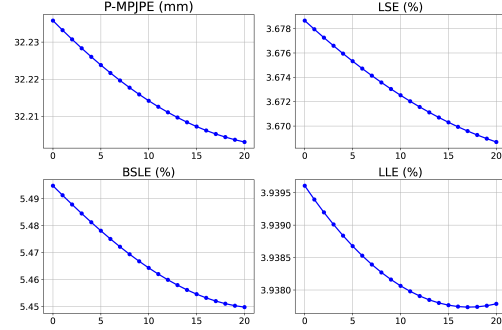


Figure 6. Gradient-Based Inference results on Human3.6M. P-MPJPE, LSE, LLE, and BSLE all decrease steadily over iterations, indicating that the loss-net effectively captures structural plausibility and provides meaningful corrective feedback to the pose-net.

consistent improvement over the strong MixSTE baseline (Table 7), suggesting that cross-window negative contrasts can provide a complementary training signal to the structural guidance of the loss-net.

Table 6. SEAL-pose on 3DHP (single-frame models). In parentheses: Δ MPJPE vs. each backbone baseline.

Setting	SimpleBaseline	SemGCN	VideoPose
SEAL-pose (Graph)	68.2 (-12.7)	62.9 (-11.6)	62.2 (-4.2)
SEAL-pose (Graph + pair-loss)	65.6 (-15.3)	62.3 (-12.2)	64.1 (-2.3)

Table 7. SEAL-pose on H36M with fixed Λ and K columns. In parentheses: Δ vs. MixSTE ($T=243$); negative is better.

Setting	Λ	K	T	MPJPE \downarrow	P-MPJPE \downarrow
MixSTE (baseline)	—	—	243	20.8	16.1
SEAL-pose (Graph margin)	10^{-3}	—	243	20.3 (-0.5)	15.8 (-0.3)
SEAL-pose (Graph margin + pair-loss)	10^{-3}	3	243	20.0 (-0.8)	15.7 (-0.4)

A.5. Simple greedy tuning protocol

In practice, we adopt a simple greedy tuning protocol:

1. We first tune the pose-net learning rate lr_p (pose-net w/o loss-net),
2. Given fixed lr_p , we explore the loss-net learning rate lr_l and energy weight α then fix the best lr_l .
3. Given fixed lr_p, lr_l , we finally tune the energy weight α .

When we apply the above greedy search, we did not observe “any” training instability. The following With a concrete example on 3DHP with VideoPose (Pavlo et al., 2019) shows the specific instance of greedy search over three hyperparameters (lr_p, lr_l, α). Please refer to Table 8. The best configuration we found was:

- pose-net lr (lr_p) = $1e-4$

- loss-net lr (lr_l) = $1e-4$
- energy weight (α) = $5e-3$

This setting yields a MPJPE of 62.18 (< 66.4 of baseline). Many nearby settings achieve very similar performance, within about 0.7 mm of the best score. Across the broader grid of learning rate and energy weight, the resulting MPJPE varies smoothly from roughly 62 mm up to approximately 67 mm as we move away from this well-tuned region, rather than collapsing or diverging. Regarding the specific question on the sensitivity to energy weight: for fixed learning rates $lr_p = lr_l = 1e-4$, sweeping α over two orders of magnitude (from $1e-4$ to $1e-2$) changes MPJPE from 62.18 mm to at most 63.82 mm. We find that energy weight α in the range of roughly $2e-3$ – $5e-3$ gives near-optimal performance, and values outside this band shift model smoothly rather than catastrophically. Similar patterns hold for other backbones and datasets.

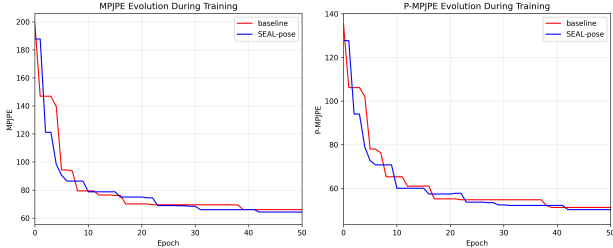


Figure 7. **Convergence comparison between the baseline and SEAL-pose during training.** Left: MPJPE, Right: P-MPJPE across epochs. Compared to the baseline (red), SEAL-pose (blue) exhibits similarly stable training dynamics while converging slightly faster, reaching comparable or lower error levels earlier.

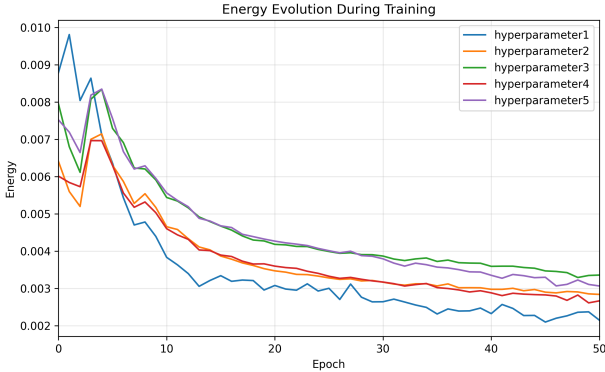


Figure 8. **Energy convergence across hyperparameter settings.** Across hyperparameters, the energy score consistently converges to a stable regime, suggesting that training remains stable and proceeds reliably after reaching a steady sub-optimal solution.

A.6. In-The-Wild Images visualization

Fig. 9, 10 shows qualitative In-The-Wild comparisons between the baseline(PoseFormerV2, KTPFormer) and SEAL-

pose. SEAL-pose often yields more structurally plausible poses, with more natural limb articulations (e.g., elbow/shoulder flexion) and more consistent left–right configurations (red/blue denote left/right), particularly for challenging poses such as hands-together or asymmetric arm motions. Overall, these visualizations suggest that incorporating the loss-net helps maintain structural consistency under noisy 2D observations.

A.7. Effect of Input Mechanism on Loss-Net Energy.

For joint j , let \mathbf{k}_j^{2D} and \mathbf{k}_j^{3D} denote the 2D and 3D keypoints, respectively. We define the coordinate vector as $\mathbf{k}_j^{\text{coord}} = [\mathbf{k}_j^{2D}, \mathbf{k}_j^{3D}]$ and use a one-hot joint label vector \mathbf{e}_j . Depending on the mechanism, the loss-net node input is either $\mathbf{h}_j = [\mathbf{k}_j^{3D}, \mathbf{e}_j]$ (3D-only) or $\mathbf{h}_j = [\mathbf{k}_j^{\text{coord}}, \mathbf{e}_j] = [\mathbf{k}_j^{2D}, \mathbf{k}_j^{3D}, \mathbf{e}_j]$ (2D–3D fused with joint labels). We evaluate four mechanisms to represent 2D/3D information for learning a 2D–3D compatibility energy.

M1 (3D-only prior) uses 3D-only inputs $\mathbf{h}_j = [\mathbf{k}_j^{3D}, \mathbf{e}_j]$ to compute a graph energy. **M2 (bilinear coupling)** forms global descriptors g_{2d} and g_{3d} from $\{\mathbf{k}_j^{2D}, \mathbf{e}_j\}_j$ and $\{\mathbf{k}_j^{3D}, \mathbf{e}_j\}_j$, and couples them via $E = \text{bilinear}(g_{2d}, g_{3d})$. **M3 (early fusion)** computes a unified graph energy on fused inputs $\mathbf{h}_j = [\mathbf{k}_j^{2D}, \mathbf{k}_j^{3D}, \mathbf{e}_j]$. **M4 (SEAL)** uses a decomposed energy $E = E_{\text{local}}(x, y) + E_{\text{global}}(y)$, where $E_{\text{global}}(y) = E(\{\mathbf{k}_j^{3D}, \mathbf{e}_j\}_j)$ and $E_{\text{local}}(x, y) = \sum_{j=1}^J (y)^\top W_j \tilde{y}$. Compared to early fusion (M3), M4 couples x and y only through the global feature, without joint-aligned 2D–3D node interactions.

Table 9 compares four loss-net input mechanisms (M1–M4) across three backbones. M3 performs best overall, achieving the lowest MPJPE on VideoPose and SemGCN, while M1 is best on SimpleBaseline. The MLP-based loss-net shows relatively consistent behavior across mechanisms, with M3 generally performing strongly. Graph-based loss-nets can represent structural dependencies more effectively by modeling joint interactions and multi-hop relational patterns, which increases their expressive power compared to an MLP-based loss-net. However, this added expressivity also makes performance more sensitive to how 2D and 3D information is injected: in our ablations, we observed slightly more rank swapping across input-mechanism variants under the graph loss-net. This sensitivity highlights that carefully designing the input mechanism is crucial for fully leveraging graph-based reasoning. Empirically, M3 performed best by exposing joint-aligned 2D–3D compatibility cues for local learning and aggregating them via message passing into a globally consistent and plausible pose energy. Overall, our input-mechanism design(M3) is not a minor implementation choice but a necessary and impactful component for 3D HPE, and the early-fusion outcome constitutes a key observation from our design process.

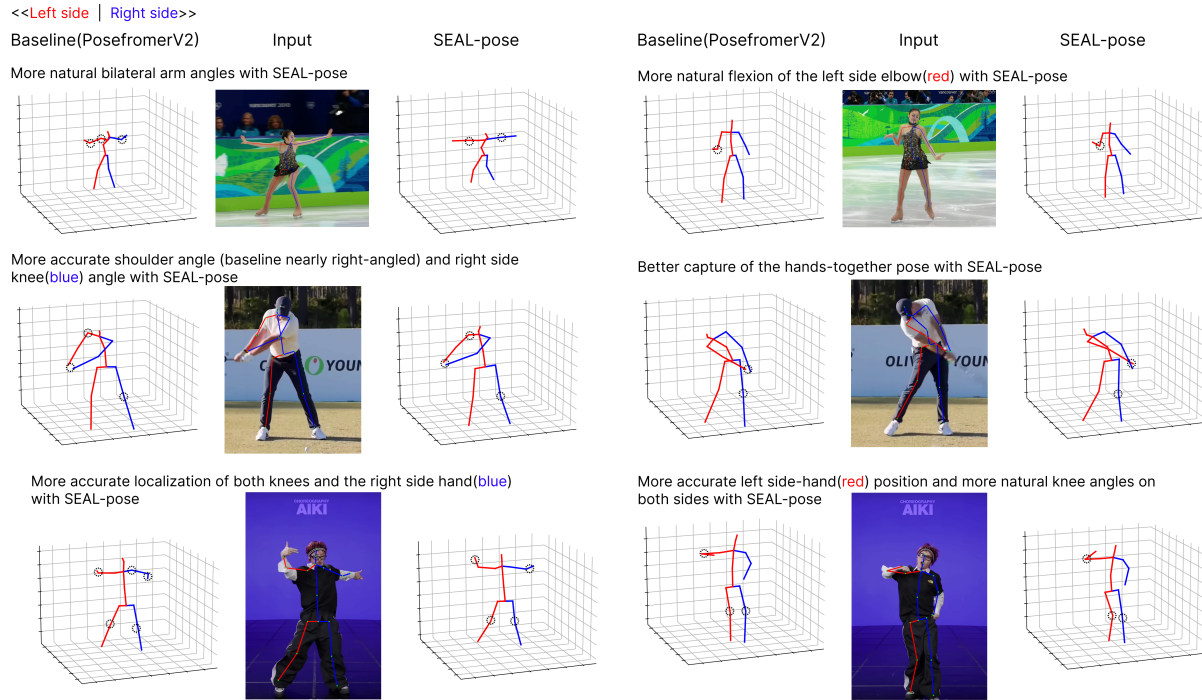


Figure 9. Qualitative Comparisons of SEAL-pose with PoseFormerV2 (Zhao et al., 2023) on In-The-Wild images. Provides visualizations on unseen In-The-Wild images, illustrating that our method produces structurally plausible poses in out-of-distribution settings.

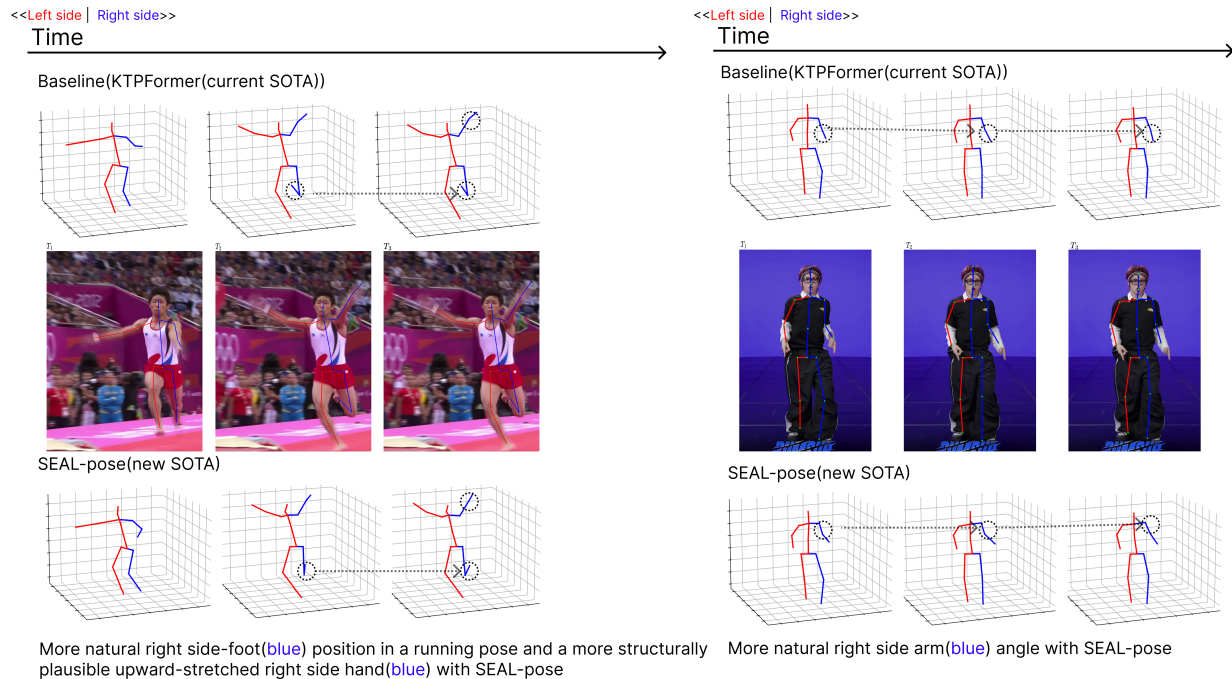


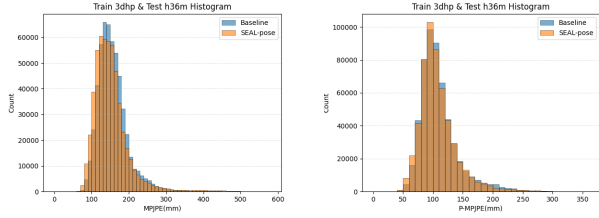
Figure 10. Qualitative Comparisons of SEAL-pose with KTPFormer (Peng et al., 2024) on an In-The-Wild Images. Provides visualizations on unseen In-The-Wild images, illustrating that our method produces structurally plausible poses in out-of-distribution settings.

pose-net lr	loss-net lr	energy weight	MPJPE
0.00010	0.00010	0.005	62.178
0.00010	0.00010	0.002	62.308
0.00005	0.00003	0.004	62.476
0.00005	0.00003	0.005	62.505
0.00010	0.00003	0.004	62.602
0.00010	0.00003	0.005	62.719
0.00010	0.00010	0.001	62.820
0.00010	0.00005	0.001	62.841
0.00010	0.00004	0.003	62.892
0.00010	0.00005	0.005	62.919
0.00010	0.00010	0.010	62.948
0.00010	0.00004	0.005	62.955
0.00010	0.00004	0.004	62.998
0.00010	0.00010	0.00050	63.072
0.00010	0.00005	0.002	63.079
0.00010	0.00010	0.003	63.085
0.00010	0.00002	0.005	63.236
0.00010	0.00002	0.001	63.276
0.00005	0.00010	0.005	63.356
0.00005	0.00010	0.004	63.365
0.00010	0.00003	0.001	63.381
0.00010	0.00003	0.003	63.479
0.00010	0.00001	0.005	63.520
0.00010	0.00002	0.004	63.554
0.00005	0.00050	0.004	63.561
0.00010	0.00010	0.004	63.570
0.00010	0.00003	0.002	63.580
0.00020	0.00003	0.004	63.693
0.00010	0.00005	0.004	63.782
0.00050	0.00010	0.001	63.789
0.00010	0.00010	0.00010	63.819
0.00020	0.00005	0.001	63.895
0.00005	0.00003	0.00050	64.006
0.00005	0.00005	0.001	64.045
0.00010	0.00004	0.006	64.092
0.00010	0.00001	0.001	64.159
0.00005	0.00003	0.00010	64.495
0.00050	0.00003	0.004	64.555
0.00005	0.00020	0.004	64.599
0.00005	0.00003	0.001	64.639
0.00005	0.00003	0.00005	64.751
0.00005	0.00003	0.00020	64.948
0.00005	0.00003	0.002	65.091
0.00020	0.00003	0.005	65.358
0.00050	0.00010	0.004	65.571
0.00050	0.00003	0.005	66.290
0.00050	0.00010	0.005	67.015
0.00002	0.00003	0.004	67.233

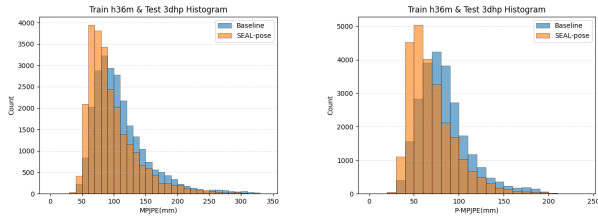
Table 8. Hyperparameter sweep over learning rates(pose-net/loss-net) and energy weight.

Table 9. MPJPE sensitivity to loss-net input designs (M1–M4). MPJPE is reported for four input designs with the backbone baseline. Best results among M1–M4 are boldfaced; Min–Max (Range) summarizes variation across designs.

Backbone	Baseline	M1	M2	M3	M4	Min–Max (Range)
SimpleBaseline	80.9	66.6	67.0	68.2	66.8	66.6–68.2 (1.6)
SemGCN	74.5	64.3	63.2	62.9	67.3	62.9–67.3 (4.4)
VideoPose	66.4	66.5	66.5	62.2	65.9	62.2–66.5 (4.3)
Avg. (3 backbones)	73.9	65.8	65.6	64.4	66.7	–



(a) Train 3DHP \rightarrow Test H36M (MPJPE / P-MPJPE).



(b) Train H36M \rightarrow Test 3DHP (MPJPE / P-MPJPE).

Figure 11. Cross-dataset error distributions in PoseFormerV2. SEAL-pose closely follows the baseline distribution and does not introduce additional degradation under dataset shift, while typically reducing the high-error tail.

A.8. Cross-dataset experiment

Fig. 11 plots error histograms (MPJPE / P-MPJPE), where each bar counts the number of test samples falling into the same error bin. Across both transfer directions, SEAL-pose shows a left-shifted distribution compared to the baseline.